Experimental and Numerical Study of Laminar-Turbulent Transition on a Low-Pressure Turbine Outlet Guide Vane

(article starts on next page)

Experimental and Numerical Study of Laminar-Turbulent Transition on a Low-Pressure Turbine Outlet Guide Vane

Isak Jonsson[1]
Department of Mechanics and Maritime Sciences,
Division of Fluid Dynamics,
Chalmers University of Technology,
Gothenburg SE 41296, Sweden
e-mail: isak.jonsson@chalmers.se

Srikanth Deshpande
GKN Aerospace Sweden,
Trollhättan SE 46181, Sweden
e-mail: srikanth.deshpande@gknaerospace.com

Valery Chernoray
Department of Mechanics and Maritime Sciences,
Division of Fluid Dynamics,
Chalmers University of Technology,
Gothenburg SE 41296, Sweden
e-mail: valery.chernoray@chalmers.se

Oskar Thulin
GKN Aerospace Sweden,
Trollhättan SE 46181, Sweden
e-mail: oskar.thulin@gknaerospace.com

Jonas Larsson
GKN Aerospace Sweden,
Trollhättan SE 46181, Sweden
e-mail: Jonas.Larsson@gknaerospace.com

This work presents an experimental and numerical investigation of the laminar-turbulent transition and secondary flow structures in a turbine rear structure (TRS). The study was executed at engine representative Reynolds number and inlet conditions at three different turbine load cases. Experiments were performed in an annular rotating rig with a shrouded low-pressure turbine upstream of the TRS test section. The numerical results were obtained using the shear stress transport $k - \omega$ turbulence model and the Langtry–Menter $\gamma - \theta$ transition model. The boundary layer transition location at the entire vane suction side is investigated. The location of the onset and the transition length are measured using IR-thermography along the entire vane span. The IR-thermography approach was validated using hot-wire boundary layer measurements. Both experiments and computational fluid dynamics (CFD) show large variations of transition location along the vane span with strong influences from endwalls and turbine outlet conditions. Both agree well with traditional transition onset correlations near midspan and show that the transition onset Reynolds number is independent of the acceleration parameter. However, CFD tends to predict an early transition onset in the midspan vane region and a late transition is present in the hub region. Furthermore, in the hub region, CFD is shown to overpredict the transverse flow and related losses. [DOI: 10.1115/1.4050629]

Keywords: aerodynamics, experimental, CFD, transition, secondary flow structures, IR thermography, turbine rear structure, low pressure turbine, engine exit structure, turbine exhaust casing, tail bearing housing, turbine rear frame

Introduction

Performance and noise requirements in modern aero-engines lead to increased bypass ratios and larger fans with a slower rotational speed. This, in turn, requires more power from the low-pressure turbine (LPT) to drive the fan. For ungeared engines, this leads to an increased number of LPT-stages with slower rotational speed. To keep the engine short each LPT-stage must have high turning which gives large swirl angles out from the last LPT-rotor. This makes the aero-design of the de-swirling LPT outlet guide vanes, located in the turbine rear structure (TRS), more challenging. For geared engines, the rotational speed of the LPT can be increased and the swirl-angle out from the last LPT-rotor will not be as high. However, increasing the bypass ratio tends to give geared engines a much larger off-design variation of the swirl-angle out from the last LPT-rotor, requiring a very robust outlet guide vane that works well for large incidence variations. This in turn also makes the aero-design of the TRS more challenging for geared engines.

This paper presents both experimental and numerical results from a detailed investigation of the flow in an engine-relevant LPT outlet guide vane structure. Earlier experimental publications related to this component are listed below. Hjärne et al. published several research papers [1–3] from linear-cascade measurements and numerical computations. Rojo et al. performed heat-transfer measurements in the linear cascade [4] and extended the scope in a new rotating LPT-stage TRS test facility [5]. The effect from

surface roughness was studied experimentally in this facility by Jonsson et al. [6] and numerically by Deshpande et al. [7]. Acoustics in a TRS was investigated by Simonassi et al. [8]. Steady-state heat transfer measurement on the outlet guide vane (OGV) was performed by Jonsson et al. [9]. The present paper investigates another important flow feature in a TRS, namely, the laminar to turbulent transition in the boundary layers on a guide vane. This work presents the first experimental verification, known to the authors, of laminar-turbulent transition in a TRS.

The transition from laminar to turbulent boundary layers is very important in turbomachinery flows, as summarized, for example, by Mayle [10] and Walker [11]. Transition affects performance and robustness toward separation, and ultimately impacts the detailed design of a guide vane. The flow in most turbine outlet guide vanes is translational, with the accelerating part on the suction side of the vane having a large laminar region and then transition somewhere after the suction peak, where deceleration and diffusion start. It is not a natural transition, occurring by growing instabilities in the laminar boundary layer. Instead, it is a bypass transition, caused by diffusion and convection of turbulent energy from the freestream into the boundary layer. Sometimes it is also possible to find laminar separation, transition, and turbulent reattachment.

The flow in a TRS is quite different from the flow in a normal LPT stage. A TRS outlet guide vane has a much lower aspect ratio (around 1) and the TRS stage consists of about 12 vanes. The upstream LPT rotor has around 70 rotor blades. Hence, wake interaction and wake-induced transition in a TRS are quite different, and correlations and models developed for an LPT stage cannot be used directly for a TRS. A TRS also de-swirls the flow and this affects the pressure gradient and creates a diffusing flow that causes an earlier boundary layer transition.

The LPT-OGV test facility [5] at Chalmers Laboratory of Fluids and Thermal Sciences used in the presented experimental work is

---

highly suitable to study transition in a TRS component. This modern facility, inaugurated in 2017, is a semi-closed rig using a rotating 1.5 stage shrouded low-pressure turbine stage to create engine-representative inlet conditions for the TRS downstream of the LPT. This facility can cover all relevant on- and off-design conditions up to a Reynolds number of 460,000.

It is important to point out that both the experimental results and the numerical studies performed in this work were done at very low Mach numbers, close to incompressible. In a real engine, the flow is compressible with an inlet Mach number around 0.5–0.6 with 0.9 at peak loaded regions. With the lack of any shocks, the main compressibility effect is in density which is well captured numerically. The main challenge is to model the boundary layer instability and the transition process. Hence, the rationale follows that a transition model that works well for the incompressible flow can be expected to work well when mitigated to flow in a real engine TRS with minor corrections. In the experimental rig the Reynolds numbers are engine relevant and the inlet boundary conditions, coming from the LPT stage upstream, are also relevant.

Approach

In order to study the transition behavior on the suction side of the TRS outlet guide vane, experiments and numerical analysis were carried out. With the Reynolds number being engine representative, incidence angles on the TRS vane are varied by changing the LPT flow coefficient, ϕ. Studies performed with three flow coefficients are presented in the present paper with 0.622 being on the design point. Flow coefficients 0.588 and 0.657 correspond to increasing and decreasing the inlet swirl angle by approximately 5 deg (decreased and increased LPT load). As all cases operate at the same Reynolds number of 235,000, the variation in inflow is due to change in turbine work extraction at a given speed, typical for a throttle variation. Earlier presented aero-thermal experimental results [6,7,9] are further analyzed and complemented with new measurement data for a better understanding of the effect of the OGV blade load on boundary layer development and secondary flow effects. Results from numerical calculations are presented in comparison to the experimental results.

Experimental Setup

The Chalmers OGV-LPT test facility is a 1.5 stage semi-closed circuit test facility that operates at approximately room temperature and pressure. The core flow is driven by a 250-kW centrifugal fan. The flow is later diffused and conditioned for uniform temperature and velocity via settling chambers, a 2 m × 2 m heat shim water cooler and a contraction. The facility operates continuously, enabling prolonged and detailed studies. The aero surfaces in the LPT and TRS are designed by GKN Aerospace, while the instrumentation and mechanical design were implemented and commissioned by Chalmers University of Technology. However, it shall be noted that the aero surfaces have been designed solely for the experimental rig and is not related to any GKN Aerospace product characteristics. Details of the facility can be obtained in previous publications [5,6,9]. Relevant features for this work are illustrated in Fig. 1. The TRS instrumentation is described in the following section.

The TRS is instrumented with two cylindrical traverse systems, one upstream of the OGV and one downstream. The downstream traverse has a long axial stroke so the two traverses together to enable 360-deg full volume access in the TRS. The standard installation is two multi-hole probes with a 5-hole probe upstream, 7-hole probe downstream, a pressure reference probe in the test section for data normalization, and pressure taps on the surface of the OGV. The axial and radial position pressure ports and evaluation planes can be seen in Fig. 2. Pneumatic data reduction methods used in this work are shown in Eq. (1) where c_p is referred to as pressure coefficient, c_{p_0} as the total pressure coefficient, and p_0^* is a
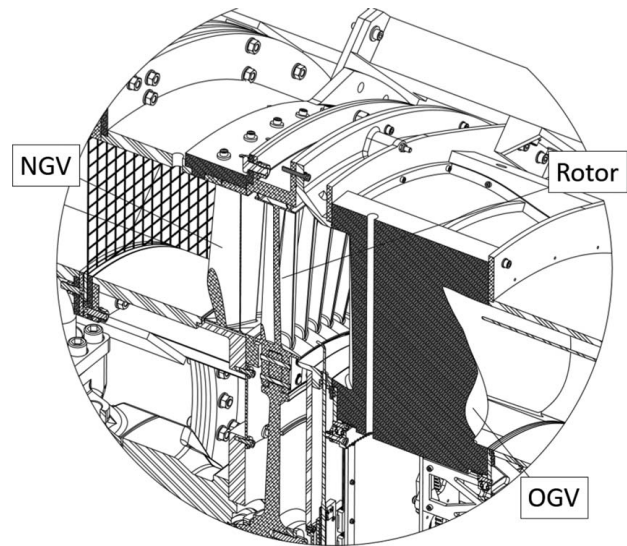

Fig. 1 Isometric section cut of the rotor, and test section showing location of nozzle guide vane, LPT rotor, and OGV

normalized total pressure. The p_{ref} and q_{ref} refer to pressure at the reference probe

$$c_p = \frac{p_i - p_{\text{ref}}}{q_{\text{ref}}}, \quad c_{p_0} = \frac{p_i - p_{0_{\text{ref}}}}{q_{\text{ref}}}, \quad p_0^* = p_{0_i} \frac{\text{avg}(p_{0_{\text{ref}}})}{p_{0_{\text{ref}}}} \quad (1)$$

Uncertainty Estimation. The uncertainties have been quantified following ASME Performance Test Codes 19.2 [12] using equal weighted error propagation shown in Eq. (2). Throughout this work, the rationale regarding uncertainty estimation, δ, of each independent variable, x_i, is included when describing the method of data collection for the sought variable ξ. The pneumatic based and IR thermographic related uncertainties can be found in Jonsson et al. [6,9] where the same setup was used

$$\epsilon_{tot}(x_1, x_2, \ldots, x_n) = \left\{ \sum_{i=1}^{n} \left(\frac{\partial \xi}{\partial x_i} \cdot \delta x_i \right)^2 \right\}^{1/2} \quad (2)$$

Infrared Thermography. In an earlier presented work by Jonsson et al. [9] one OGV with internal water channels was installed to measure steady-state heat flux by forced convection. These internal water channels circulate warm water at a relatively high speed and mass-flow to provide a near-constant inner wall temperature. The air side of the OGV is unevenly cooled by force convection and radiation causing a surface temperature change which is measured via IR thermography. To isolate background radiation and increase camera sensitivity and accuracy, the vane is coated with Nextel 6081 coating and 2–3 mm diameter gold-leaf
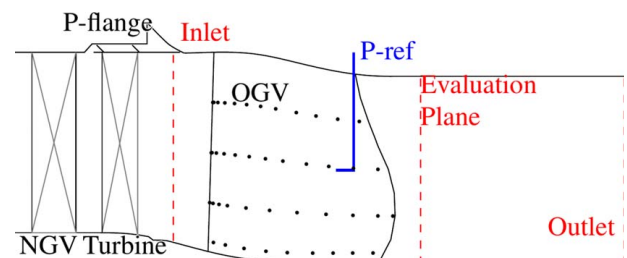

Fig. 2 Axial and radial location of the evaluation planes, pressure taps, and reference probe P-ref

markers. The gold-leaf markers also provide geometrical references for mapping the camera images onto the OGV surface.

A FLIR Phoenix 320 camera is used for thermal measurements, sensitive to mid-wave infrared spectrum at 3–5 nm. The camera has a full frame sample rate of 120 Hz and a resolution of 320×264 pixels. From in-house calibration, the noise equivalent temperature difference was found to be less than 15 mK at a surface temperature around 25 °C which is the average surface temperature for experiments conducted in this study. The camera is mounted outside the wind tunnel downstream of the OGV and enables a clear view of the OGV up to $x/c \geq 0.15$ with less than a 55 deg surface normal view angle.

Most transition detection methods using IR thermography do not directly use quantitative heat transfer but rather a qualitative approach from a heat transfer perspective. This is done by using a semi-uniform input heat flux such as external lights as shown by Gardner et al. [13] or internal surface heating as shown by Simon et al. [14]. By using the Reynolds analogy assuming constant heat flux, temperature variations on the surface can be related to skin friction. Hence, as skin friction varies throughout the boundary layer development so will the surface temperature. Furthermore, the unsteady nature in transition causes variation of surface temperature which can be detected if the temperature difference surpasses the sensitivity of the camera. Commonly used methods for analyzing this signal are differential infrared thermography as shown by Merz et al. [15], temperature fluctuations or using a sliding subtracting frame as in Gardner et al. [16]. In this work, a new variable σ_T is introduced as it was found to be the most practical viable parameter to indicate transition. σ_T is defined in Eq. (3) where Y_i is camera counts after camera non-uniformity compensation. The minimum and maximum values are the extreme points in the proximity of the transition. The temperature has been normalized with T_n which is based on temperature extremes in the proximity of transition, shown in Eq. (4).

$$\sigma_T = \frac{\sigma_{Y_i} - \sigma_{Y_i, \min}}{\sigma_{Y_i, \max}}, \quad \sigma_{Y_i} = std(Y_i) \quad (3)$$

$$T_n = \frac{\Delta T_{surf} - \Delta T_{surf, \min}}{\Delta T_{surf, \max} - \Delta T_{surf, \min}}, \quad \Delta T_{surf} = T_{surf} - T_{air} \quad (4)$$

Uncertainty for $T_n \pm 0.045$ K in this work is in proportion to uncertainties in steady-state heat flux presented in Jonsson et al. [9]. This uncertainty estimation is very conservative as it accounts for independent variables not required for ΔT_{surf}.

Hot-Wire Measurements. For the boundary layer velocity profile and intermittency, γ a single-wire hot-wire probe with a 3 mm long $5\,\mu m$ diameter wire with a maximum frequency response of 10 kHz was used with a Dantec CTA 56C17 anemometer and a NI-4461 for data acquisition. Calibration was done in house before and after measurements using the same calibrator as detailed in a previous work by Rojo [5].

The velocity profile was used to calculate momentum thickness, θ, used for the momentum thickness Reynolds number, Re_θ, similar to Mayle [10], as detailed in Eq. (5) where the subindex t denotes the onset of the transition. The acceleration parameter, K, was calculated using Eq. (6), where the dU_t/dx can be rewritten using static pressure along the surface, the assumption of incompressibility and Bernoulli's principle. The intermittency identification was done as demonstrated by Chernoray [17].

$$Re_{\theta_t} = \theta_t U_t / \nu \quad (5)$$

$$K_t = \frac{\nu}{U_t^2} \frac{\partial U_t}{\partial x} = -\frac{\nu}{\rho U_t^3} \frac{\partial p}{\partial x} \quad (6)$$

Flow Visualization. Flow visualization was performed using a mixture of kerosene, SAE 40 oil, and titanium oxide pigment. An image was captured every 30 s to trace the development and point of stabilization. To ease comparison with numerical results, images from experiments were projected on the OGV surface using the software BLENDER™ 2.81 and UV mapping. The process is shown in Fig. 3 moving from left to right. Note that streamlines are based on many trials with different mixtures to study different areas of interest. More details of the different load cases can be found in Vikhorev et al. [18].

Numerical Setup

The three-dimensional numerical analysis of a single passage sector is carried out using the commercial software FLUENT™ R19.1. The CFD context model is built using a commercial modeling tool. A sector blade is modeled using the hexahedral mesh. ICEMCFD™ is used for meshing. The mesh size of the sector is around 2 million nodes which is based on a grid sensitivity analysis. The boundary layer refinement was done with a target y-plus of 1 on all wall boundaries. The mesh distribution on the wall boundaries is as shown in Fig. 4.

Steady-state Reynolds-Averaged Navier–Stokes Simulation (RANS) simulations are performed with a correlation-based transition shear stress transport (SST) model. The model is based on
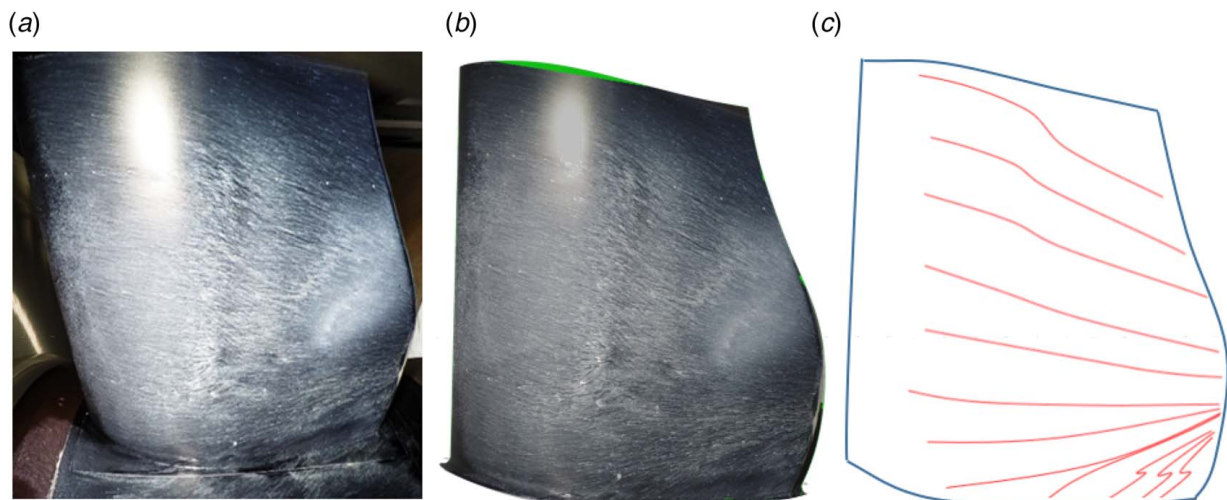

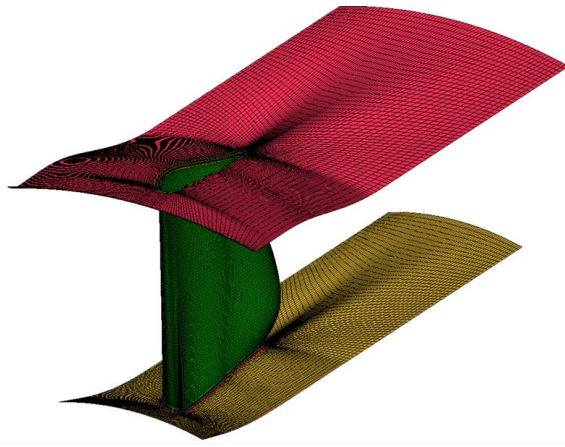Fig. 3 Flow visualization with (*a*) raw images, (*b*) projected view, and (*c*) only streamlines

Fig. 4 Mesh distribution on wall boundaries

Fig. 5 Inlet swirl α and normalized total pressure p_0^* from experiments used at the inlet boundary

two transport equations ($\gamma - \theta$ model), one for the intermittency and one for the transition onset criteria in terms of momentum thickness Reynolds number. The detailed model definition can be found in the publication by Menter et al. [19]. FLUENT[TM] v19.1 provides options to customize the transition length function, critical momentum thickness Reynolds number, and transition onset momentum thickness Reynolds number. In this paper, the results are based on the default settings for transition. Possible modifications of these parameters, based on the comparison of results, are considered for future work. For the present work, wall boundaries are defined as non-adiabatic. This definition of non-adiabatic walls helps to capture the temperature variations on the vane surface. Temperature distribution on the vane surface is compared to the data from measurements in order to study the onset of transition on the OGV surface. A temperature difference of the order of 20 K was maintained between the inlet temperature and wall temperature.

The experimental data from the 5-hole probe and the 7-hole probe at the inlet and the evaluation plane, respectively, are used as boundary conditions for numerical analysis. The locations of these planes are shown in Fig. 2. The numerical domain is extended to the outlet. The stagnation boundary conditions and flow direction for the analysis are derived from measured experimental data. The turbulence properties at the inlet are taken from a multistage simulation including the upstream LPT stage, which is present in the experimental setup. The distributions along the span of the inlet for the normalized total pressure, p_t^*, are shown in Fig. 5. Each flow coefficient corresponds to a different incidence angle to which the TRS vane is exposed. The profiles tend to be relatively more hub-strong with increasing flow coefficients. Moreover, the total pressure gradient from hub to shroud decreases with an increase in flow coefficient.

The swirl angle variation that is measured at the inlet of the TRS is used for numerical simulations. The swirl angle variation with change in flow coefficient is shown in Fig. 5. The spanwise variation of the inlet swirl angle for each flow coefficient is in the order of 40–50 deg. Flow coefficients are chosen in the way that the swirl angle variation is in the steps of 5 deg. The points close to the outer case wall do not fall in line with the other points in swirl variation. This is due to the tip leakage effect. The rotor upstream of the TRS is shrouded and the tip leakage effect is taken into consideration in order to study the aerodynamic behavior of the TRS. It is of interest to determine whether the numerical methodology will be able to capture the effects of the tip leakage flow, even though there is only a single point measuring the flow variables in the region affected by the tip leakage flow at the inlet. One of the objectives of the TRS is to de-swirl this inlet swirl and maximize the axial component of momentum for maximum thrust.
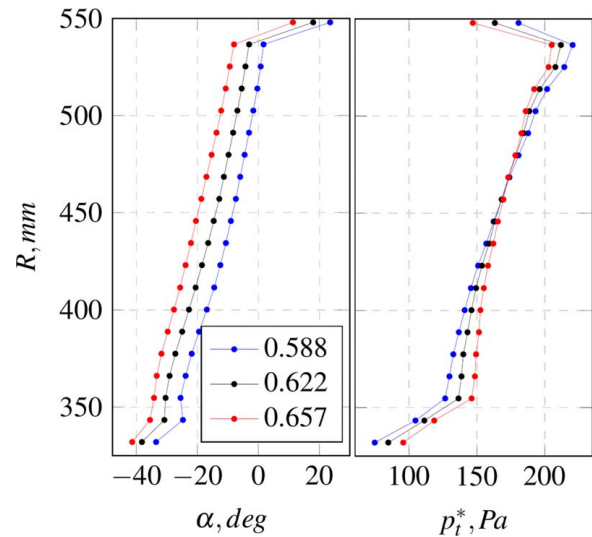
At the exit, the average static pressure value from the experiments is used as a boundary condition. The average static pressure, during the numerical analysis, is monitored and changed in order to maintain the same pressure as in the experiments.

Results

The vanes in the TRS are of a low aspect ratio and, therefore, secondary flows become dominant and it is of interest to study the effect of transition on secondary flows. However, as a first step, transition studies are presented at the midspan location where primary flow effects are assumed to be dominant. Later, the analysis is expanded to include the secondary flow where the same analysis is applied to the full span on the suction side in combination with both numerical and experimental surface streamlines. Finally, the outlet plane is studied where the performance of the OGVs is evaluated by wake analysis.

Blade Loading. One of the primary flow effects on transition onset on the suction side is the acceleration rate, and thus, it is important that numerical and experimental blade loading are coherent. The suction side blade loading at midspan is shown in Fig. 6 which can be correlated to the acceleration rate using Eq. (6). Numerical results of c_p are shown as solid lines and symbols are used for experimental data. The blade loading does, in general, have a good agreement between numerical and experimental results. Three observations can be made with increased turbine
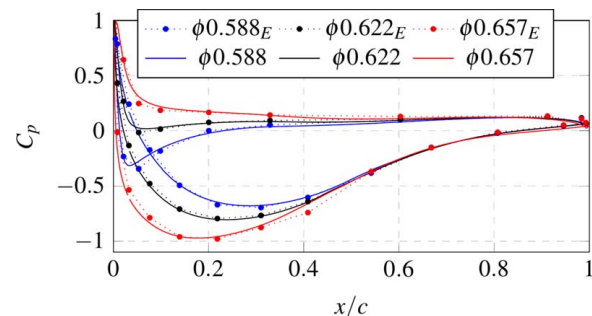

Fig. 6 Blade loading comparison at midspan for different ϕ for numerical (solid lines) and experimental results (symbols with dotted lines)

flow coefficient, ϕ, (i) blade loading increases, (ii) suction peak moves downstream chord wise, and (iii) pressure recovery rate $\partial p/\partial x$ after the suction peak increases. At $x/c = 42\%$ for a flow coefficient of 0.657, the experimental results show a delayed suction peak pressure recovery that is not seen in numerical simulations.

Free-Stream Turbulence Levels. Another primary cause of transition onset is the free-stream turbulence. Far free-stream turbulence measurements in the TRS from previous work [6] are shown in Fig. 7 along x/c with averaged free-stream turbulence displayed as a solid line and the 95 percentile as a shaded area. The measurement was done in the center of the passage between two OGVs. Figure 7 shows the decay of the turbulence through the TRS, from a $Tu = 4.6\%$ at the inlet to $Tu = 2.1\%$ at the most aft-wards data point.

Temperature Profile and Variations at Midspan. The two variables σ_T and T_n are used for comparison of transition prediction of numerical tools and observed transition in experiments using the rationale presented in section Infra Red Thermography. Figures 8–10 show the normalized differential temperature T_n at the suction side midspan along the chord for both numerical T_{n_N} and experimental data T_{n_E} as well as the unsteady surface temperature variation σ_T. For the design point, i.e., $\phi = 0.622$, shown in Fig. 8 the experimental data demonstrate noticeable high values of temperature fluctuations in the range of 40– 57% of span. The cause of these high values is attributed to high temporal skin friction variations in the transition area. The axial chord where this transition occurs is marked by blue shaded rectangle in the figure. The temperature profile supports transition occurring in the same region with an onset at 40% of span. The numerical temperature profile T_{n_N} indicates an onset at $x/c = 0.15$ upstream of the experimental results. The temperature fluctuations σ_T and T_n at $\phi = 0.588$ are shown at midspan in Fig. 9. Both the numerical and the
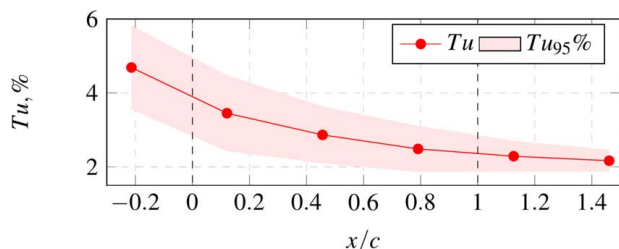

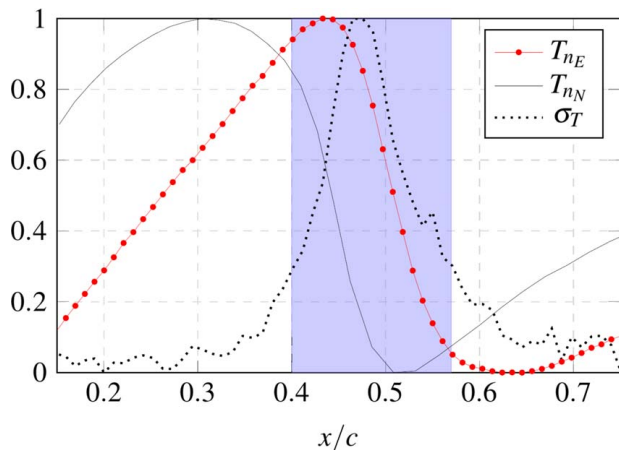Fig. 7   Free-stream turbulence in the TRS along x/c at $\phi = 0.622$

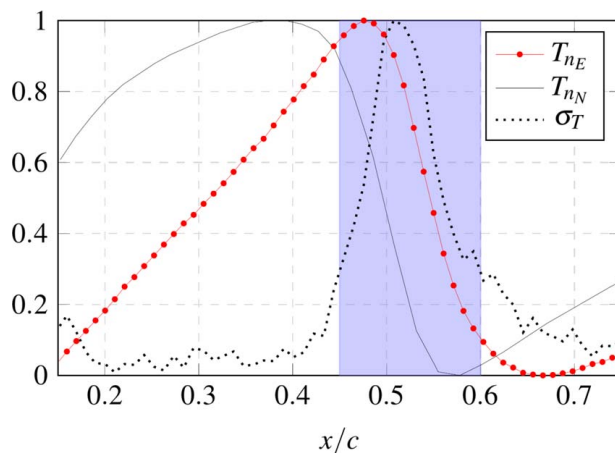Fig. 8   Chordwise T_n variation at $\phi = 0.622$ at midspan for numerical and experimental data along with σ_T distribution

Fig. 9   Chordwise T_n variation at $\phi = 0.588$ at midspan for numerical and experimental data along with σ_T distribution
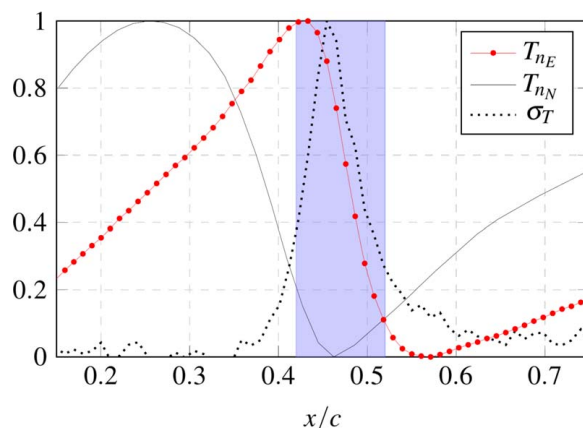

Fig. 10   Chordwise T_n variation at $\phi = 0.657$ at midspan for numerical and experimental data along with σ_T distribution

experimental T_n are similar to the case for $\phi = 0.622$ with the difference of an experimental aft-ward shift of $x/c = 0.05$, indicating a later transition onset for the lower flow coefficient. Compared with the two other cases, the case for $\phi = 0.657$ shown in Fig. 10 has larger discrepancy between numerical and experimental data. At $\phi = 0.657$ the experimental data show an aft-wards transition location at $x/c = 0.42$ while the numerical data show a front-shifted location at $x/c = 0.22$. Experiments also indicate a more rapid transition compared to all other cases with a shorter range of peak to peak T_n and $\sigma_T \geq 0.3$. The delayed pressure recovery seen at $x/c = 0.42$ in Fig. 6 for $\phi = 0.657$ is at the same location as experimentally indicated transition onset from T_{n_N} and σ_T.

Boundary Layer at Midspan. Results from σ_T and T_n at midspan for $\phi = 0.622$ in Fig. 8 indicate that the onset of transition is at $x/c = 0.4$ and that the boundary layer would be fully turbulent at $x/c = 0.6$. In order to verify the actual boundary layer state, a hot-wire probe was used. From the hot-wire measurement the velocity and intermittency γ profiles at midspan at $x/c = 0.4, 0.5, 0.59$ are shown in Figs. 11(a) and 11(b). Boundary layer at point $x/c = 0.4$ shows a typical laminar velocity profile with low values of intermittency indicating that it is at the very start of the transition. Boundary layer at point $x/c = 0.5$ illustrates an inflectional velocity profile that is inconclusive individually, but with intermittency results, it can be argued to indicate early to mid-transition as the intermittency values are relatively high. At point $x/c = 0.59$ the boundary layer is fully turbulent, seen both as velocity profile shape and intermittency.
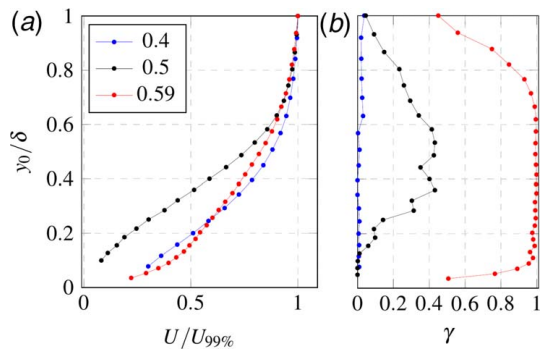
Fig. 11 Hot-wire boundary layer measurement on the midpan across estimated transition location from σ_T: (a) velocity profile and (b) intermittency

To relate the midspan results with existing correlations and experimental data, the data are presented as shown by Mayle [10] using the momentum thickness Reynolds number Re_{θ_t} and the acceleration parameter K_t in Fig. 12. Figure 12 shows the effect of the acceleration parameter on the onset of transition with the momentum thickness Reynolds number. The region above the stability criterion, formulated by Thwaites [20], shows where a laminar boundary layer would separate in low-turbulence flow. The three dashed lines in Fig. 12 show $Re_{\theta_t} = 400Tu^{(5/8)}$ as formulated by Mayle for three different turbulence levels and shows that an increased freestream turbulence decreases Re_{θ_t} and the Re_θ dependency.

Experimentally Re_{θ_t} and K_t were calculated using Eqs. (5) and (6). The exact point of the transition onset x_t/c is challenging to identify. One commonly used method is defined by Narasimha [21] but this requires a higher density of axial data points than available. With lack of these, the location of onset is motivated by boundary layer results at $x/c = 0.4$ for $\phi = 0.622$ and expanded to other cases using temperature fluctuations σ_T. Blade loading in Fig. 6 shows that all the cases have a positive K_t upstream of the suction peak. Blade loading also shows that an increased ϕ causes higher flow acceleration at the suction peak with a stronger deceleration (lower K_t) downstream of the peak. In Fig. 12, Re_{θ_t} and K_t are shown as red markers for the numerical results and blue markers for experimental results, vertical lines are used for the acceleration parameter at $\phi = 0.588$ and $\phi = 0.657$ as the momentum thickness is unknown.

The experimental boundary layer data for $\phi = 0.622$ match well with correlations for a turbulence level of $Tu = 2.75\%$ and $K_t = -1.36 \times 10^{-6}$. Observed transition onset for $\phi = 0.588$ from T_{n_N} and σ_T indicates a lower acceleration parameter, which by

Table 1 Observed and predicted Re_θ at $\phi = 0.622$ including error estimation with impact from independent variables in descending order

Source	Re_θ	Dependency and uncertainty
Experiments	220 ± 15	$\theta \pm 0.01$ mm, U_t, ν
CFD	$226 \pm -$	$-$
Mayle [10]	215 ± 10.5	$Tu \pm 0.2\%$

following the above-mentioned correlations should be a by-pass transition for similar Re_θ. Using the same rationale, the acceleration parameter for $\phi = 0.657$ is outside the weights stability criterion and, hence, the likelihood of separation-induced transition is increased. Blade loading and temperature studies support this. Firstly, the delayed suction peak recovery seen in Fig. 6 $x/c = 0.42$ occurs close to the indicated transition onset surface temperature shown in Fig. 10. Secondly, Fig. 10 shows a shorter transition length for $\phi = 0.567$ indicating a separation-induced transition. The location of the numerical transition point was selected using T_N following the same rationale as for the experimental results. The numerical results show similar Re_θ at the transition point but as the transition onset occurs on a different x/c, and hence, there are variations in the acceleration parameter K_t. The largest discrepancy is found at $\phi = 0.657$ with a much lower acceleration value at transition onset, Re_{θ_t}.

Table 1 compares Re_θ at $\phi = 0.622$ from experiments with numerical results and correlation from Mayle [10]. When possible, the uncertainty is specified in the second column and the independent variable contribution in descending order in the third column of Table 1.

Full-Span Comparison. Figure 13 shows the suction side of an OGV with streamlines from flow visualization as red lines and numerical streamlines as black lines. Along with these, $\sigma_T \geq 0.3$ is illustrated as a blue field to indicate transition in the same manner as for earlier presented midspan data. The two dashed black lines show the predicted location of transition onset and ending from numerical simulations based on surface temperature distribution. For all cases, streamlines near hub and shroud deviate toward midspan which creates a decelerated zone as the streamtubes expand. Numerical and experimental streamlines are in good agreement near and above 50% span for all cases. However, numerical results show a more profound streamline curvature for all cases near the hub, causing a larger spanwise extent of hub separation. The effects are more profound with increased OGV load and with increased secondary flow structures. In the vicinity of this flow at case $\phi = 0.622$ and $\phi = 0.657$ high values of σ_T can be found, which is caused by the spanwise movement of the separation line. At higher blade loading this causes a local separation and the unsteady nature of this phenomena causes the spanwise unsteadiness.

At $\phi = 0.588$ and $\phi = 0.622$, the predicted and observed transition agree well with a nearly constant early prediction of a by-pass transition except near the hub and shroud. Near the wall, an increased ϕ causes a spanwise aft-ward climb of the transition point for both numerical and experimental data. The growth angle relative to the hub and shroud lines is more profound in experimental results. The location of the transition point at the hub leading edge is critical for downstream secondary flow propagation but no σ_T values are available in this area. When running a rich flow visualization with a low viscosity mixture at $\phi = 0.657$, a weak cross flow could be detected marked as a thin dotted red line. The flow propagates along the most of the span moving from shroud toward the hub line and exiting at 30% span. This cross-flow feature was not observed at the other two ϕ. At midspan, the weak cross-flow is located upstream of the observed separation-induced transition onset. It is common to observe an early separation-induced transition in flow visualization due to the interaction with the liquid
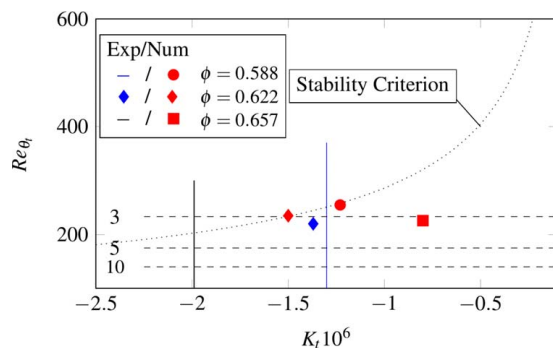

Fig. 12 The Reynolds number of transition onset as a function of the acceleration parameter at transition. Current experimental and numerical data (points and vertical solid lines) compared to previous correlations (dashed lines). See text for further details
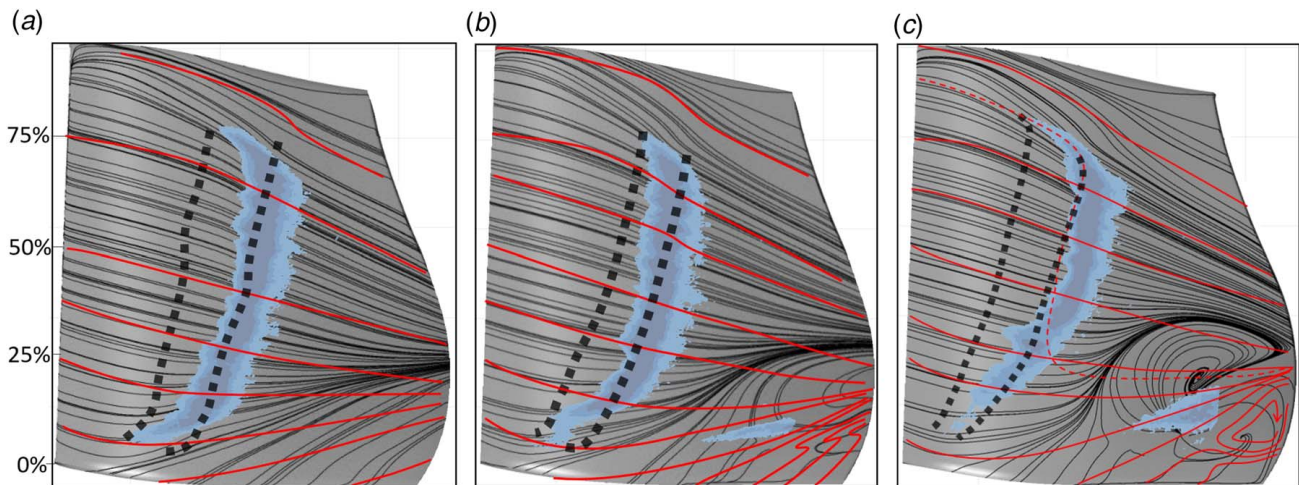
Fig. 13 Comparison of numerical and experimental streamlines and transition location following the same rationale as for midspan on the entire suction side at different load cases. Numerical results are shown as solid black lines for streamlines and dashed for the onset and end of transition. Red lines represent observed flow streaklines from flow visualization and transition location from IR-thermography as blue contours. (a) $\phi = 0.588$. (b) $\phi = 0.622$, and (c) $\phi = 0.657$.

and it further supports that a large portion of span transition at $\phi = 0.657$ is separation induced.

Wakes. Figure 14 shows c_{p_0} at the outlet from the three different load coefficients where the OGV wakes are seen from downstream the TRS module. The wakes are wider near the hub both due to a larger wetted area with a thicker and longer airfoil and due to a hub strong blade loading. However, for most cases the larger losses near the hub are due to the secondary flow and with increased ϕ the secondary losses become prominent and impact the wake

growth disproportionately near the walls. For all cases, the numerical tool does slightly underpredict wake width for the center and upper span, but near the hub it overpredicts the secondary flow structures and losses. One reason the secondary flow structures at the shroud are underpredicted in numerical results could be due to that only one data-point was available to describe the tip clearance flow and, hence, there is a slight difference in inlet conditions. As the inlet to the numerical simulations is circumferential averaged, no traces of upstream stator wakes can be observed but the overall flow redistribution is well captured.

Conclusions

Both numerical and experimental results have been used in the endeavor to better understand the transition prediction on an OGV suction side at a variety of typical LPT operational conditions. The experimental study was done in a realistic engine-like environment in Chalmers University of Technology 1.5 stage LPT-OGV test facility at a Reynolds number of 235,000. The study covers variation of the inlet swirl by ± 5 deg from the design condition. The numerical study was performed with a commercial CFD code using the SST $k - \omega$ turbulence model and the Langtry–Menter transition model. Experimental circumferentially averaged inlet pressure and flow angles are used as boundary conditions for numerical simulations. Turbulence properties at the inlet are taken from a multistage simulation including the upstream LPT stage.

Transition onset localization using IR thermography has successfully been implemented for the first time in a TRS test facility running at engine representative conditions. This method provides near full span transition onset location and length from both temperature mean and fluctuation magnitude. The transition area, from onset to end was defined as the location where 30% of peak temperature fluctuation was observed. The IR thermography predicted onset and transition length is shown to agree with a traditional approach relying on hot-wire intermittency measurements. The average temperature profile was further used to compare numerical and experimental data for transition onset and length. The highest and the lowest average temperature values in the proximity to the transition location represent well the onset and ending of transition respectively.

The results show that the inlet swirl variation from hub to shroud leads to a hub strong OGV load. The inlet spanwise variations is affecting the transition chorwise location, but near the end walls the transition onset is primarily affected by the secondary flow. As the OGV is higher loaded near the hub, the secondary flow is
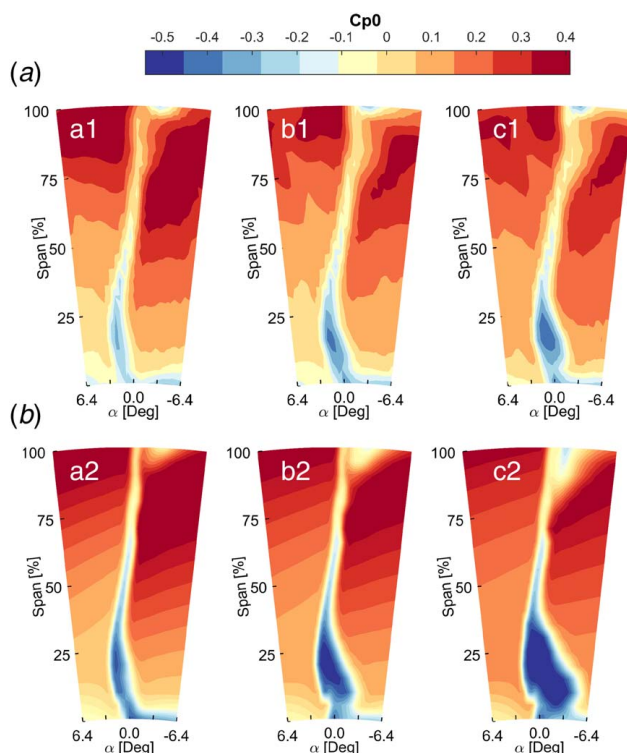

Fig. 14 Wake Comparison of (a) numerical and (b) experimental results with flow coefficient (a1, a2) $\phi = 0.588$, (b1, b2) $\phi = 0.622$, and (c1, c2) $\phi = 0.657$

more profound in this region which correlate to the loss distribution observed in wake studies. Comparison of numerical and experimental results shows that the $\gamma - \theta$ model is able to predict the transition onset spanwise distribution. An early prediction can be observed near the midspan region while a late transition in the hub region. Numerical simulations capture trends in the transition location movement in the streamwise direction caused by turbine flow coefficient variations. Even though the transition onset moves aft-wards with decreased OGV loading, both the numerical and the experimental results correlate well with traditional transition onset correlations based on the momentum thickness Reynolds number and turbulence levels. For the investigated transition points the momentum Reynolds number is independent of the acceleration parameter. However, the mode of transition and momentum thickness are influenced by the acceleration parameter.

Conflict of Interest

There are no conflicts of interest.

Data Availability Statement

The authors attest that all data for this study are included in the paper.

Nomenclature

p = static pressure
q = dynamic pressure
K = acceleration parameter
U = velocity
c_{p_0} = total pressure coefficient
c_p = static pressure coefficient
p_0 = total pressure
y_0 = wall distance
T_n = normalized temperature
Y_i = IR-camera counts
Re = Reynolds number
Re_θ = momentum thickness Reynolds number
T = temperature
Tu = turbulence intensity
α = swirl angle
γ = intermittency
θ = momentum thickness at transition onset
σ_T = normalized surface temperature fluctuations
ϕ = flow coefficient

Abbreviations and Subscripts

E = experimental data/results
N = numerical data/results

References

[1] Hjärne, J., Chernoray, V., and Larsson, J., 2008, "Experimental Investigations and Numerical Validation of an Outlet Guide Vane With an Engine Mount Recess," ASME Turbo Expo, Berlin, Germany, June 9–13, pp. 989–998.

[2] Hjärne, J., Larsson, J., Chernoray, V., and Löfdahl, L., 2007, "Numerical Validations of Secondary Flows and Loss Development Downstream of a Highly Loaded Low Pressure Turbine Outlet Guide Vane Cascade," ASME TURBO EXPO, Montreal, Canada, May 1–11, pp. 723–733.

[3] Hjärne, J., Larsson, J., and Löfdahl, L., 2006, "Performance and Off-Design Characteristics for Low Pressure Turbine Outlet Guide Vanes: Measurements and Calculations," ASME Turbo Expo 2006, Barcelona, Spain, May 8–11, pp. 649–658.

[4] Rojo, B., Jimenez, C., and Chernoray, V., 2014, "Experimental Heat Transfer Study of Endwall in a Linear Cascade With IR Thermography," EPJ Web Conf., 67(1), p. 2.

[5] Rojo, B., 2017, "Aerothermal Experimental Investigation of LPT-OGVs," PhD Thesis, Chalmers University of Technology, Gothenburg.

[6] Jonsson, I., Chernoray, V., and Rojo, B., 2018, "Surface Roughness Impact on Secondary Flow and Losses in a Turbine Exhaust Casing," Proceedings of ASME Turbo Expo 2018. ASME Paper No. GT2018-75541.

[7] Deshpande, S., Jonsson, I., and Chernoray, V., 2019, "Effect of Surface Roughness on Aerodynamic Performance of Turbine Rear Structure," Proceedings of ASME Turbo Expo 2019. ASME Paper No. GT2019-90472.

[8] Simonassi, L., Zenz, M., Zerobin, S., Selic, T., Heitmeir, F., and Marn, A., 2019, "On the Influence of An Acoustically Optimized Turbine Exit Casing Onto the Unsteady Flow Field Downstream of a Low Pressure Turbine Rotor," ASME J. Turbomach., 141(4), p. 041003.

[9] Jonsson, I., Chernoray, V., and Dhanasegaran, R., 2020, "Infrared Thermography Investigation of Heat Transfer on Outlet Guide Vanes in a Turbine Rear Structure," Int. J. Turbomach. Propulsion Power, 5(3), p. 23.

[10] Mayle, R. E., 1991, "The 1991 IGTI Scholar Lecture: The Role of Laminar-Turbulent Transition in Gas Turbine Engines," ASME J. Turbomach., 113(4), pp. 509–536.

[11] Walker, G. J., 1993, "The Role of Laminar-Turbulent Transition in Gas Turbine Engines: A Discussion," ASME J. Turbomach., 115(2), pp. 207–216.

[12] ASME International, A., 2005, Test Uncertainty PTC 19.1," Technical Report, ASME International.

[13] Gardner, A. D., Eder, C., Wolf, C. C., and Raffel, M., 2017, "Analysis of Differential Infrared Thermography for Boundary Layer Transition Detection," Exp. Fluids, 58(9), p. 122.

[14] Simon, B., Filius, A., Tropea, C., and Grundmann, S., 2016, "IR Thermography for Dynamic Detection of Laminar-Turbulent Transition," Exp. Fluids, 57(1), pp. 1–12.

[15] Merz, C., Richter, K., and Raffel, M., 2014, "Differential Infrared Thermography for Unsteady Boundary-layer Transition Measurements," AIAA. J., 52(9), pp. 2090–2093.

[16] Gardner, A. D., Wolf, C. C., and Raffel, M., 2016, "A New Method of Dynamic and Static Stall Detection Using Infrared Thermography," Exp. Fluids, 57(9), p. 149.

[17] Chernoray, V., 2015, "Prediction of Laminar-Turbulent Transition on An Airfoil At High Level of Free-stream Turbulence," 5th European Conference for Aeronautics and Space Sciences, Munich, Germany, July.

[18] Vikhorev, V., Chernoray, V., Thulin, O., Deshpande, S., and Larsson, J., 2020, "Detailed Experimental Study of the Flow in a Turbine Rear Structure at Engine Realistic Flow Conditions," Proceedings of ASME Turbo Expo 2020. ASME Paper No. GT2020-15734.

[19] Menter, F. R, Langtry, R. B., Likki, S. R., Huang, P. G., and Völker, S., 2006, "A Correlation-Based Transition Model Using Local Variables–Part I: Model Formulation," ASME J. Turbomach., 128(3), pp. 413–422.

[20] Thwaites, B., 1949, "Approximate Calculation of the Laminar Boundary Layer," The Aeronautical Quarterly, 1(3), pp. 245–280.

[21] Narashimha, R., 1957, "On the Distribution of Intermittence in the Transition Region of a Boundary Layer," J. Aero. Sci., 24(1), pp. 711–712.